

Analysis of rotor eddy current loss and thermal deformation of magnetic liquid double suspension bearing^①

LIU Hongmei (刘洪美)^{*}, YANG Guang^{**}, SUN Yanan^{**}, SUN Jian^{**}, WANG Zhe^{***}, ZHAO Jianhua^{②***}

(^{*} Shijiazhuang Rail Transit Group Co. Ltd, Shijiazhuang 050011, P. R. China)

(^{**} Shijiazhuang Haishan Industrial Development Co. Ltd, Shijiazhuang 050200, P. R. China)

(^{***} Fluid Power Transmission and Control Laboratory, Yanshan University, Qinhuangdao 066004, P. R. China)

Abstract

Magnetic-liquid double suspension bearing (MLDSB) is a new type of suspension bearing based on electromagnetic suspension and supplemented by hydrostatic supporting. Without affecting the electromagnetic suspension force, the hydrostatic supporting effect is increased, and the real-time coupling of magnetic and liquid supporting can be realized. However, due to the high rotation speed, the rotor part produces eddy current loss, resulting in a large temperature rise and large thermal deformation, which makes the oil film thickness deviate from the initial design. The support and bearing characteristics are seriously affected. Therefore, this paper intends to explore the internal effects of eddy current loss of the rotor on the temperature rise and thermal deformation of MLDSB. Firstly, the 2D magnetic flow coupling mathematical model of MLDSB is established, and the eddy current loss distribution characteristics of the rotor are numerically simulated by Maxwell software. Secondly, the internal influence of mapping relationship of structural operating parameters such as input current, coil turns and rotor speed on rotor eddy current loss is revealed, and the changing trend of rotor eddy current loss under different design parameters is explored. Thirdly, the eddy current loss is loaded into the heat transfer finite element calculation model as a heat source, and the temperature rise of the rotor and its thermal deformation are simulated and analyzed, and the influence of eddy current loss on rotor temperature rise and thermal deformation is revealed. Finally, the pressure-flow curve and the distribution law of the internal flow field are tested by the particle image velocimetry (PIV) system. The results show that eddy current loss increases linearly with the increase of coil current, coil turns and rotor speed. The effect of rotational speed on eddy current loss is much higher than that of coil current and coil turns. The maximum temperature rise, minimum temperature rise and maximum thermal deformation of the rotor increase with the increase of eddy current loss. The test results of flow-pressure and internal trace curves are basically consistent with the theoretical simulation, which effectively verifies the correctness of the theoretical simulation. The research results can provide theoretical basis for the design and safe and stable operation of magnetic liquid double suspension bearings.

Key words: magnetic-liquid double suspension bearing (MLDSB), oil film thickness, current loss, thermal deformation, particle image velocimetry (PIV) test

0 Introduction

Magnetic-liquid double suspension bearing (MLDSB) is a new type of support bearing combining the electromagnetic suspension and the liquid hydrostatic support. On the basis of not affecting the electromagnetic force, the hydrostatic support effect is increased, and the real-time coupling supporting of elec-

tromagnetic suspension and hydrostatic support can be realized. The carrying capacity and stiffness are significantly improved, and the operation stability and the service life can be increased^[1].

During the operation process, the rotor cuts the magnetic inductance at high speed, a large amount of eddy current loss can be generated, then the temperature rise and the thermal deformation of the rotor occur. Since the design gap between the magnetic pole

① Supported by the Natural Science Foundation of Hebei Province (No. E2020203052) and the S&T Program of Hebei (No. 236Z1901G).

② To whom correspondence should be addressed. E-mail: zhaojianhua@ysu.edu.cn.

Received on Nov. 2, 2023

and the rotor is only 30 μm , the thermal deformation of the rotor can lead to the change of the thickness of the oil film, and the bearing capacity and stiffness of liquid film are reduced. The phenomenon of ‘holding shaft’ and ‘burning tile’ will occur, the safe and stable operation of MLDSB are restricted, and the service life can be shortened^[2-3].

At present, many experts and scholars have conducted in-depth research on the eddy current loss, and achieved the fruitful research results. Refs [4,5] investigated the effects of rotor sheath material, thickness and number of axial segments on eddy current losses. The results showed that reducing the thickness of the sheath and increasing the number of axial segments could effectively reduce the eddy current loss. The titanium alloy TC4 was beneficial for reducing eddy current losses and effectively protecting permanent magnets. Refs [6,7] investigated the generation mechanism and calculation method of eddy current loss in permanent magnet motor windings. The results showed that the computational speed of the method was improved by nearly 100 times and the error was less than 5% over a large frequency range. Refs [8-10] designed a new type of super magneto strictive transducer and calculated the rare earth rod eddy current loss of the transducer. The results showed that the eddy current loss of untreated rare-earth rods was mainly concentrated on the outer diameter surface. The eddy current loss of sliced rare-earth rods was reduced by 67.9%. A fast-analytical model for the rotor eddies current loss of a surface-mounted permanent magnet synchronous motor with a protective sheath was proposed by Refs [11-13]. They considered three cases, namely stator temporal harmonics, eddy current backlash, and circumferential segmentation of the permanent magnets. It was shown that the present analytical model could quickly obtain the response surface of eddy current loss, which provided a theoretical basis for motor design and optimization iteration. Ref. [14] established a multi-physical field simulation model of permanent magnet high-speed solenoid valve with electric, magnetic and mechanical fields. The results showed that the eddy current loss was positively correlated with the material conductivity, and the magnetic saturation strength was negatively correlated with the conductivity. Refs [15-17] analyzed the relationship between the variation rule of magnetic field and eddy current loss of permanent magnet for two kinds of built-in V-type and double-V-type rotor permanent magnet synchronous motors under different weak magnetic conditions. The results showed that the motor with double V-rotor structure had 28% larger

convexity, good weak magnetic properties and 40% smaller eddy current loss of permanent magnet magnets.

Compared with the conventional electromagnetic bearings, electric motors, solenoid valves, the distribution of electromagnetic coil and the cooling channel of MLDSB are special and complicated, and it is subjected to the coupling influence of magneto-liquid-thermo-solid multiple physical fields. So the mechanism and influence law of eddy current loss of MLDSB are unclear^[18-19]. Therefore, this paper explores the eddy current loss mechanism, temperature rise and thermal deformation of MLDSB, and analyzes the internal influence of input current, coil turns and rotor speed on eddy current loss.

1 Magnetic fields and eddy model

1.1 3D model of magnetic field

The 3D model of the MLDSB is shown in Fig. 1. According to its structural characteristics and current direction, 2D model is established as shown in Fig. 2.

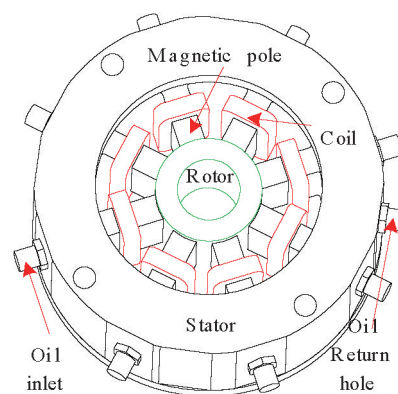


Fig. 1 3D model of MLDSB

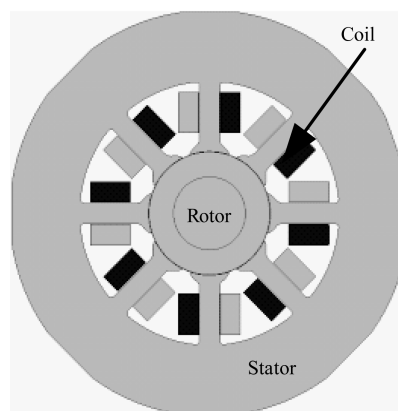


Fig. 2 2D model of calculation domain

The computational model of MLDSB includes fluid and solid domains. Only solid domains, such as stator, coil, rotor and spindle, are considered in the calculation process.

The initial design parameters of MLDSB are shown in Table 1.

Table 1 Initial design parameter of MLDSB

Initial current i_0/A	Initial rotational speed $n/(r \cdot \text{min}^{-1})$	Wire diameter E/mm	Conductivity $\rho_0/(\Omega \cdot \text{m}^{-1})$	Rotor width C/mm
1.72	1 000	0.4	0.133	55.0
Turns of coil $N/\text{dimensionless}$	Coil length L/m	Pole width A/mm	Rotor inner diameter B/mm	Rotor outer diameter D/mm
265	19.5	20.0	45.0	65.0

The calculation domain can be simplified as follows.

- (1) Ignore the threads and replace the rounded corners with right angles.
- (2) Ignore the part which do not affect the calculation results, including the end caps on both sides and the skeleton seal.
- (3) Ignore the shoulder on the rotor, and intercept only part of the rotor.
- (4) Ignore the magnetic leakage.

The computational domain includes five materials: air, stator, rotor, spindle, and coil. The stator and rotor are magnetic materials, and the relative permeability of the air and the coil is 1.0.

Set $A_z = 0$, and zero magnetic potential is loaded at the outer boundary as shown in Fig. 3.

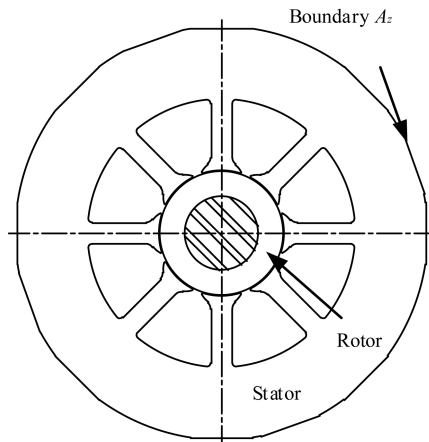


Fig. 3 Boundary of MLDSB

1.2 2D model of eddy field

The material properties of MLDSB are shown in Table 2.

Table 2 Material of MLDSB

Parameter	Stator (23QG385)	Coil (Cu)	Rotor (23QG385)
Elasticity modulus E/MPa	1.95×10^5	1.1×10^5	1.95×10^5
Expansion coefficient $\beta/(\mu\text{m}/^\circ\text{C})$	11.2	18.5	11.2

Since the rotor is in a rotating state, it is set as moving area in Fig. 4.

Due to the different winding ways, the magnetic poles show NSSNNSN distribution and each adjacent magnetic pole forms a pair of magnetic flux loops.

The eddy current losses can be generated when the rotor cuts magnetic inductance line at high speed. Set the zero current direction for the rotor as shown in Fig. 5.

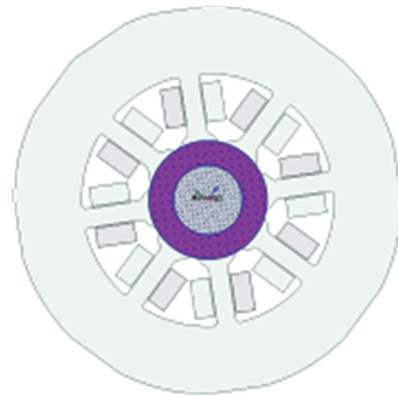


Fig. 4 Rotation zone

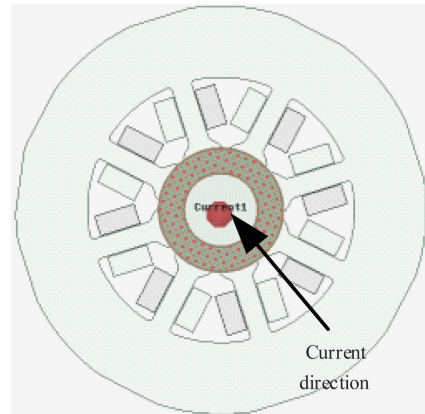


Fig. 5 Current excitation

2 Analysis of eddy current loss

2.1 Simulation of eddy current loss

According to Tables 1 – 2, the distribution of the magnetic induction strength and the eddy current of MLDSB are simulated, and the results are shown in Figs 6 – 7.

As shown in Fig. 6, each magnetic pole is connected with an enameled coil and the winding mode of each coil is controlled. The magnetic pole surface is arranged in NSSNSSN mode. Each two adjacent magnetic poles are a pair and each pair of magnetic poles and the magnetic sleeve forms the magnetic flux loop. It is basically consistent with the theoretical design.

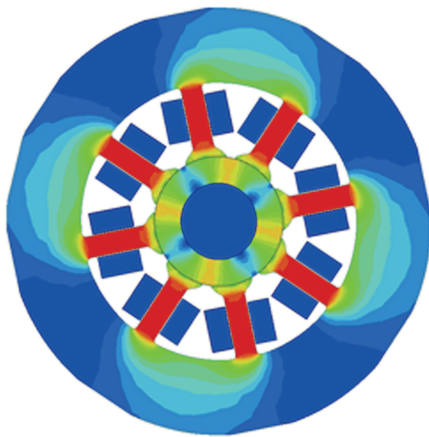


Fig. 6 Magnetic induction intensity



Fig. 7 Eddy distribution

From Fig. 7, it can be seen that a large amount of eddy current loss occurs when the rotor cuts the magnetic inductance line at high speed. Eddy current losses are concentrated on the surface of the rotor, and it is basically consistent with the engineering practice.

2.2 Influence of input current on eddy current loss

The initial input current is assumed to be 1.72 A, 2.22 A, 2.72 A, 3.22 A and 3.72 A, the eddy current loss curve is shown in Fig. 8.

From Fig. 8, it can be seen that the eddy current loss is 45 W at 1.72 A. As the current increases to 2.22 A, 2.72 A, 3.22 A and 3.72 A, the eddy current loss increases to 50 W, 52 W, 56 W and 60 W, respectively. With the increase of the current, the eddy current loss increases gradually at a proportionate rate.

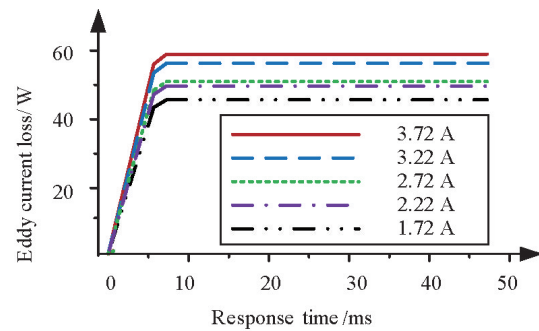


Fig. 8 Eddy current loss on different current

The influence of input current on eddy current loss is shown in Fig. 9.

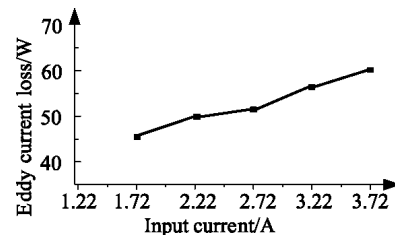


Fig. 9 Effect of current on eddy current loss

From Fig. 9, it can be seen that with the increase of the input current, the eddy current loss increases at a proportionate rate.

2.3 Influence law of coil turns on eddy current loss

When coil turns are 265, 315, 365 and 415, the eddy current loss is obtained as shown in Fig. 11.

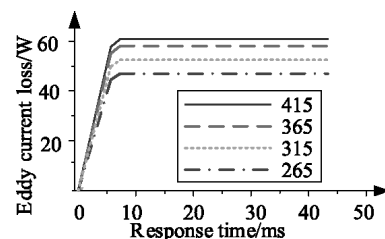


Fig. 10 Eddy current loss on different coil turns

From Fig. 10, it can be seen that the eddy current loss is 45 W, 50 W, 56 W and 60 W when the turns of the coil are 265, 315, 365 and 415, respectively. With the increase of coil turns, the eddy current loss increases.

The influence of coil turns on eddy current loss are summarized as shown in Fig. 11. It can be observed that the eddy current loss of the rotor increases with the increase of coil turns.

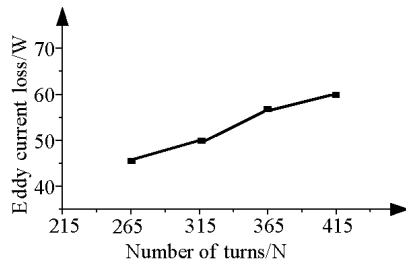


Fig. 11 Effect of coil on eddy current loss

2.4 Effect of rotational speed on eddy current loss

The rotational speed is set to $1\,000\text{ r}\cdot\text{min}^{-1}$, $1\,500\text{ r}\cdot\text{min}^{-1}$, $2\,000\text{ r}\cdot\text{min}^{-1}$, $2\,500\text{ r}\cdot\text{min}^{-1}$, correspondingly the eddy current loss curves at different rotational speeds are shown in Fig. 12.

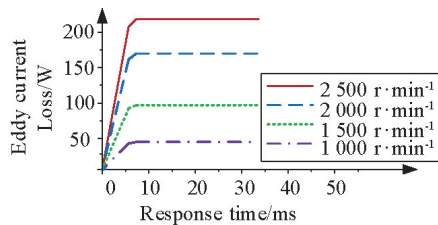


Fig. 12 Eddy current loss on different rotational speed

As shown in Fig. 12, the eddy current loss is 45 W, 98 W, 170 W and 240 W when the rotational speed increase to $1\,000\text{ r}\cdot\text{min}^{-1}$, $1\,500\text{ r}\cdot\text{min}^{-1}$, $2\,000\text{ r}\cdot\text{min}^{-1}$, and $2\,500\text{ r}\cdot\text{min}^{-1}$, respectively.

The influence of rotational speed on eddy current loss is shown in Fig. 13.

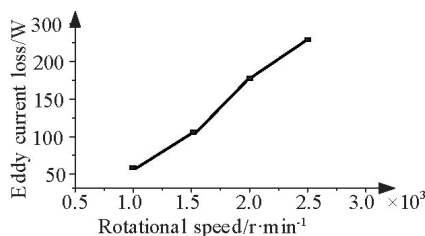


Fig. 13 Effect of rotational speed on eddy current loss

It can be seen from Fig. 13 that the rotor eddy current loss increases linearly proportionality with the

increase of the input current.

By comparing Fig. 9, Fig. 11 and Fig. 13, it can be got that when the input current increases from 1.72 A to 3.72 A, the coil increases from 265 turns to 415 turns and the rotational speed increases from $1\,000\text{ r}\cdot\text{min}^{-1}$ to $2\,500\text{ r}\cdot\text{min}^{-1}$, the eddy current losses increases by 15 W, to 95 W, respectively.

3 Thermal deformation simulation

3.1 Effect of eddy current loss on temperature rise

Based on the input current of 1.72 A, rotational speed of $1\,000\text{ r}\cdot\text{min}^{-1}$ and coil turns of 265, the eddy current loss of the rotor is calculated to be 45 W. Consequently, for simulation purposes, the eddy current loss is set at 45 W, 70 W, 95 W, and 160 W, as shown in Table 3.

Number	1	2	3	4
Eddy current loss/W	45	70	95	160

The eddy current loss is used as the heat source, the temperature distribution cloud map of rotor is obtained as shown in Fig. 14.

From Fig. 14, it can be seen that the temperature is centrally symmetrical, increases along the lateral direction and the temperature rise is mainly concentrated in the edge parts. The temperature rise at the oil outlet is low, and the temperature increases gradually with the exit distance. The temperature on the bus is distributed symmetrically. Because the liquid flow speed in this region is fast and the cooling efficiency is high, so the middle temperature rise is low and the region is relatively uniform. Because the cooling speed and efficiency is low on the bus side, so the edge temperature is high and the temperature rise is large.

The temperature rise of the rotor is shown in Fig. 15. It can be seen that with the increase of the eddy current loss, the maximum and minimum temperature rise increase synchronously.

3.2 Effect of eddy current loss on thermal deformation

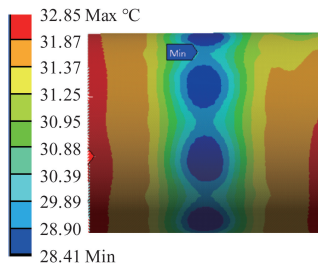
Similarly, the thermal deformation is simulated as shown in Fig. 16. From Fig. 16, it can be seen that the thermal deformation is centrally symmetric, and increases from the center to the outside along the direction of the bus. The thermal deformation at the edge is the largest, at the outlet is lower than other parts of the shell. Because the flow rate of the outlet is faster, the cooling effect is higher, so the thermal distortion away from the outlet gradually increases.

The thermal deformation on the bus is symmetri-

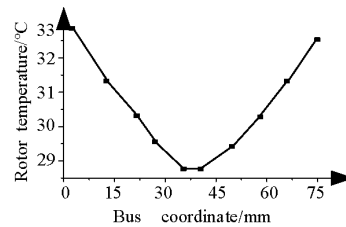
cally distributed. Because the middle area is close to the inlet, the flow speed is fast, the cooling efficiency is high. And then the thermal deformation is low and uniform. While the both side area are far away from the outlet, so the flow speed is slow, the cooling effi-

ciency is low, the temperature is high and then the thermal deformation is larger. It is necessary to improve the cooling efficiency of the both side area.

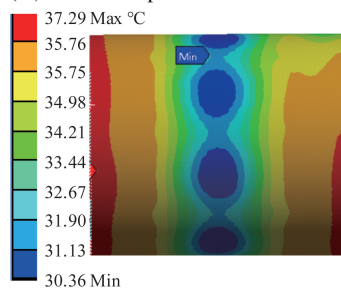
Similarly, the thermal deformation curve is shown in Fig. 17.



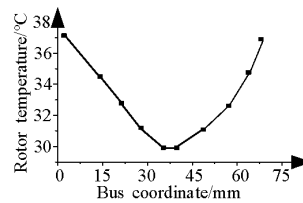
(a) Rotor temperature at 45 W



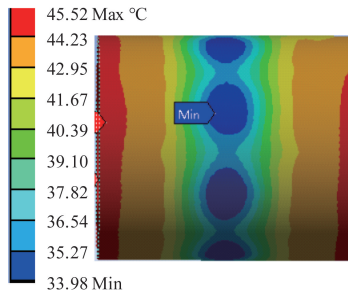
(b) Bus temperature at 45 W



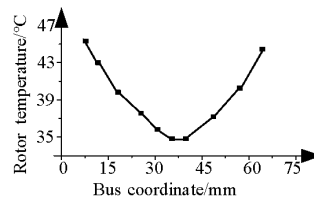
(c) Rotor temperature at 70 W



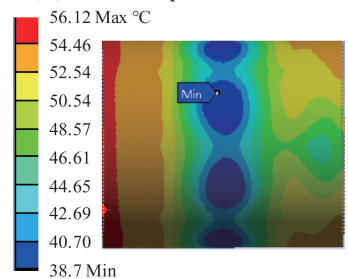
(d) Bus temperature at 70 W



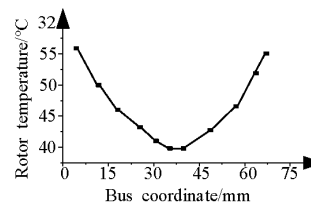
(e) Rotor temperature at 95 W



(f) Bus temperature at 95 W

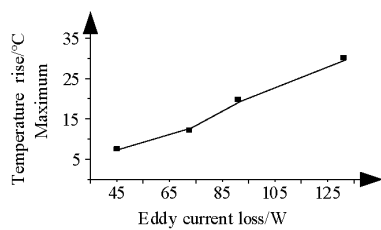


(g) Rotor temperature at 130 W

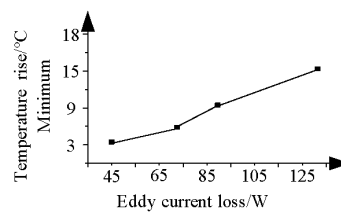


(h) Bus temperature at 130 W

Fig. 14 Temperature of rotor on different eddy current loss



(a) Maximum temperature rise curve



(b) Minimum temperature rise curve

Fig. 15 Temperature rise on different eddy current loss

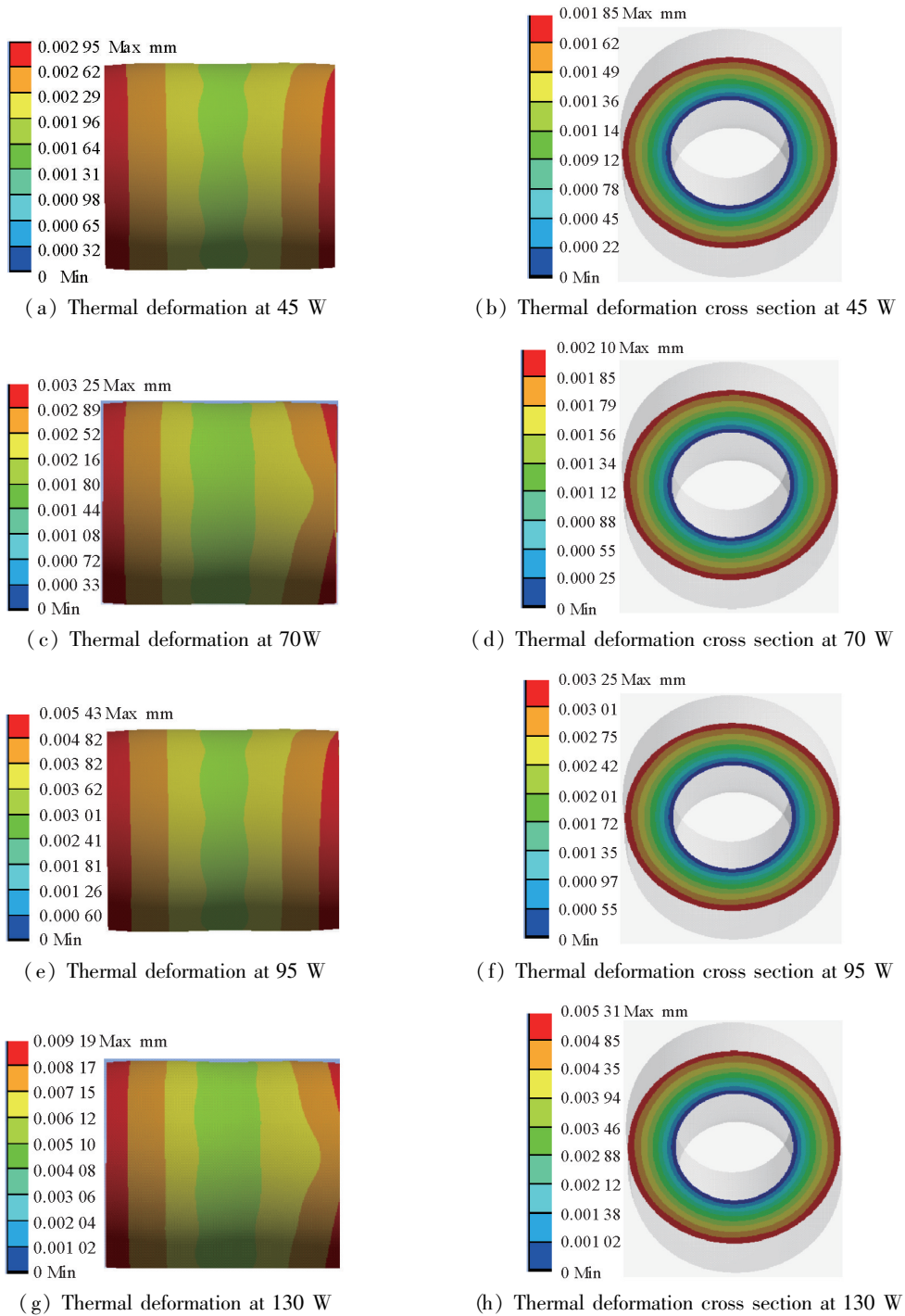


Fig. 16 Thermal deformation on eddy current loss

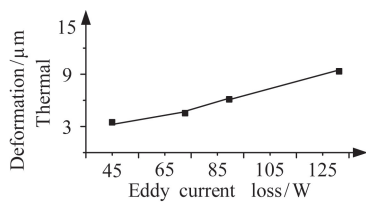


Fig. 17 Thermal deformation

From Fig. 17, it can be seen that the maximum thermal deformation of the rotor increases with the in-

crease of the eddy current loss.

4 Experimental validation

4.1 Introduction to PIV test system

The particle imaging velocity measurement system mainly consists of four parts: light source system, imaging system, tracer particle system and image acquisi-

tion system, as shown in Fig. 18.

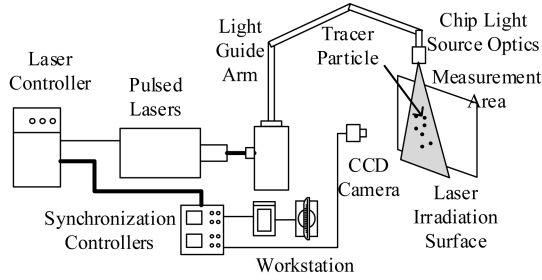


Fig. 18 PIV system

The laser model is Vlite-200 and its parameters are shown in Table 4.

Table 4 Parameter of pulse generator

Model	Supply voltage	Output wavelength	Output energy
Vlite-200	220 V	532 nm	200 mJ
Repetition rate	Pulse width	Energy stability	Dispersion angle
1 - 15 Hz	≤ 8 ns	$\leq 2\%$	≤ 3 rad

4.2 MLDSB test setup

The end cap and stator are made of plexiglass material with strong light transmittance. The dimensions of the stator are shown in Table 5.

Table 5 Plexiglass model of MLDSB

Pole width A/mm	Pole length B/mm	Enface area S1/mm ²	Coil cavity area S/mm ²
20	45	887.8	437.1

The dimensions and photo of stator are shown in Fig. 19 and Fig. 20. The observation area shown in Fig. 20 is the sector between two magnetic poles. The observation area is 10 mm away from the inlet and outlet plane.

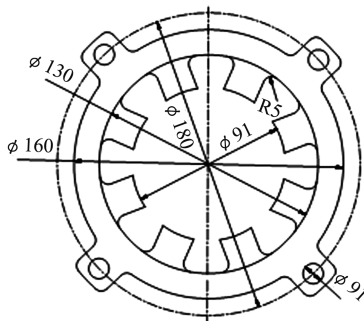


Fig. 19 Dimension of stator

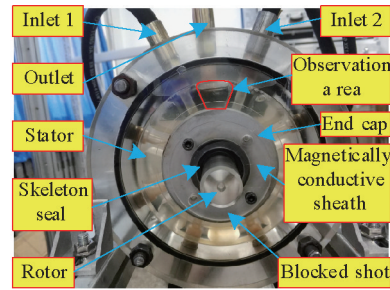


Fig. 20 Plexiglass model photo of MLDSB

During the experiment process, the water mixed with the tracer particles flows through Inlets 1 and 2. The flow can be regulated by throttle valve. Flowmeters and pressure gauges are respectively installed at Inlet 1 and Inlet 2 in order to monitor the pressure and flow rate of the water.

The pressure-flow test system is shown in Fig. 21.

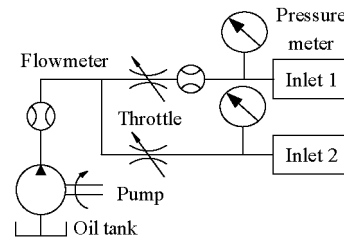


Fig. 21 MLDSB flow test system

The key parameters of each component are shown as follows.

(1) The model of needle valve is J13W-160P. Its diameter is 6 mm, the material is 304 stainless steel, and the manufacturer is Wenzhou Qixin Valve Co., LTD.

(2) The model of the pump is QDX1.5-15-0.37. Its lift is 15 m, the rated power is 0.37 kW and the manufacturer is Shanghai Qiantao Company.

(3) The range of the pressure gauge is 0.02 - 0.60 MPa.

(4) The model of the flowmeter is HBG-F8500A10131. Its measuring medium is water, the range is $0.028\ 300 - 205\ 258\ \text{m}^3 \cdot \text{h}^{-1}$, and the manufacturer is Xiamen Heisenberg Electric Co., LTD.

4.3 Test procedure for observation

(1) Close the camera cover, set the laser to the appropriate width of sheet light, and set the sheet light to the plane to be measured.

(2) Place the scale into the plane to be measured, and switch off the laser source and open the

camera cover.

(3) Open the observation software and adjust the camera focus so that the scale can be clearly photographed.

(4) Camera calibration: switch off the laser, select 'Single frame mode' to capture 1 picture, switch to 'Acquired Data' column and click 'Save for Calibration'.

(5) Switch to analyze mode, right-click on the captured picture to open the Measurement Scale Factor option, drag the two points AB in the picture to both ends of the scale, and enter the distance between the two-points AB shown on the scale in the 'Absolute Distance' column.

(6) Add a filter to the camera and switch the laser to external trigger mode.

(7) Watch the value of the pressure gauge to set the inlet pressure and adjust the flow rate of the pump, as shown in Table 6.

(8) Switch to the acquisition mode → select 'Double frame mode' → enter the appropriate time interval → enter the acquisition frequency → enter the number of pictures collected → click 'Acquire' to collect pictures → switch to 'Acquired Data' column → click 'Save in Database'.

(9) After the acquisition and storage are completed, switch to the analysis mode and carry out analysis.

(10) Record the pressure gauge and flowmeter indication, collect photos and analyze them.

Table 6 Inlet pressure of MLDSB

Number	1	2	3	4	5	6
Inlet 1 pressure /MPa	0.04	0.04	0.06	0.06	0.08	0.10
Inlet 2 pressure /MPa	0.00	0.04	0.00	0.06	0.08	0.10

Adjust the inlet pressure until the flow meter is stable. The CCD camera continuously takes dynamic photos of the flow field in the marked area in Fig. 20 and records the flowmeter indicator.

4.4 Pressure-flow test results

Adjust the inlet pressure according to the data in Table 6 and record six groups of flow rate data as shown in Table 7.

Table 7 Flow rate when different inlet pressure

Number	1	2	3	4	5	6
Pressure /MPa	0.040	0.040	0.060	0.060	0.080	0.100
Inlet 1 Test flow rate / (L · min ⁻¹)	0.817	0.833	1.233	1.217	1.650	2.083
Simulation flow rate / (L · min ⁻¹)	0.883	0.883	1.333	1.333	1.767	2.217
Pressure /MPa	0.000	0.040	0.000	0.060	0.080	0.100
Inlet 2 Test flow rate / (L · min ⁻¹)	0.000	0.800	0.000	1.183	1.633	2.033
Simulation flowrate / (L · min ⁻¹)	0.000	0.883	0.000	1.333	1.767	2.217
Test total flow rate / (L · min ⁻¹)	0.817	1.633	1.233	2.400	3.283	4.116
Simulation total flowrate / (L · min ⁻¹)	0.883	1.766	1.333	2.666	3.534	4.434

The experimental pressure-flow relationship is compared with the simulation curve as shown in Fig. 22 and Fig. 23.

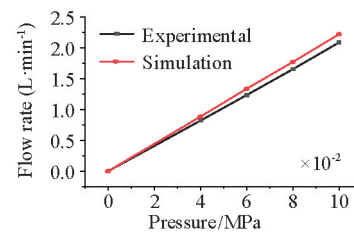


Fig. 22 Flow of Inlet 1

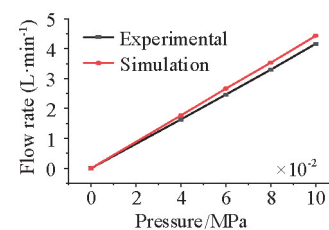


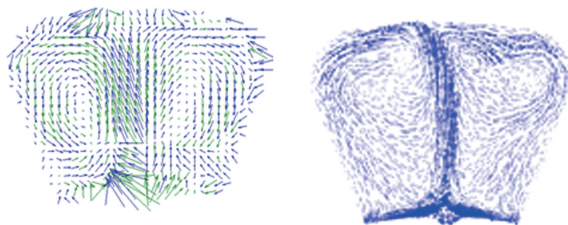
Fig. 23 Total flow rate of two inlets

From Fig. 22 and Fig. 23, it can be seen that the flow rate of Inlet 1 and total flow rate increase linearly with the increase of inlet pressure. Due to the processing errors, the inner diameter accuracy of the plexi-glass stator is low, and the design gap between the rotor and the stator is less than the theoretical liquid film thickness. So, the simulation results are slightly larger than the test results, but the variation trend is basically the same.

4.5 Results of PIV experimental

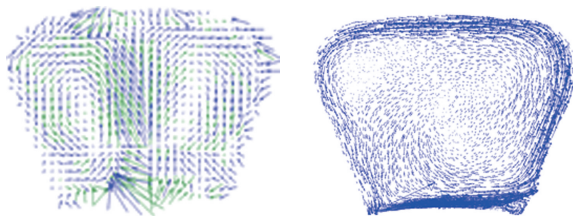
The PIV image of vector diagram of the internal flow field is compared with the simulation results as shown in Figs 24 – 28.

From Figs 24 – 28, it can be observed that the simulation internal flow trace is almost consistent with the experimental results. When the inlet pressure at both ends is 0.04 MPa, 0.06 MPa and 0.08 MPa respectively, two vortices are generated in the internal flow field, and the fluid flows upward in the middle of the eddy. When Inlet 1 is only open, there is only one eddy and its position is random. With the increasing of the inlet pressure, the trend of the track is roughly the same and there is no great change.



(a) Experimental curve (b) Simulation curve

Fig. 24 Trace when Inlets 1 and 2 are 0.04 MPa



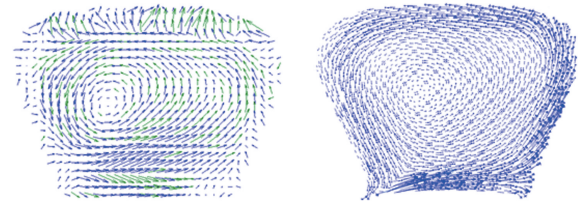
(a) Experimental curve (b) Simulation curve

Fig. 25 Trace when Inlet 1 is 0.04 MPa and Inlet 2 is 0.00 MPa



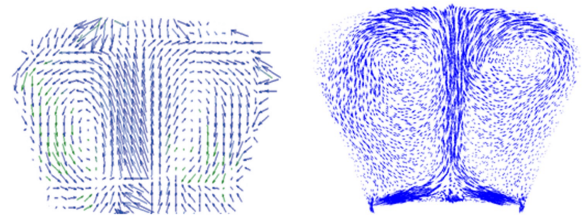
(a) Experimental curve (b) Simulation curve

Fig. 26 Trace when Inlets 1 and 2 are 0.06 MPa



(a) Experimental curve (b) Simulation curve

Fig. 27 Trace when Inlet 1 is 0.06 MPa and Inlet 2 is 0.00 MPa



(a) Experimental curve (b) Simulation curve

Fig. 28 Trace when Inlet 1 and Inlet 2 are 0.08 MPa

5 Conclusion

(1) Rotor's eddy current loss increases linearly with the increase of coil current, coil turns and rotor speed.

(2) The rotor speed affects the eddy current loss to a much greater extent than the coil current and the coil turns.

(3) As the eddy current loss increases, the maximum temperature rises and thermal deformation of the rotor increases.

(4) The flow-pressure and internal traces of MLDSB are tested, which effectively verifies the correctness of the theoretical simulation.

References

- [1] YU A D, PU S, et al. Research on the combined machine tool for processing automobile automatic transmission box [J]. *Machine Tool and Hydraulics*, 2018, 46(8): 25-28, 57.
- [2] CHEN Y. Research on usability of numerical control lathe [D]. Harbin: Harbin Engineering University, 2012. (In Chinese)
- [3] HU X F, LIU G, SUN J J, et al. Analysis of eddy current loss in axial magnetic bearings [J]. *Bearing*, 2013(3): 22-27.
- [4] LIU K, ZHOU Y, YANG X B, et al. Influence of the structure of high-speed permanent magnet synchronous motors on eddy current loss of rotor [J]. *Small & Special Electrical Machines*, 2022, 50(12): 16-20, 26.
- [5] TONG W M, HOU M J, SUN L, et al. Analytical method of rotor eddy current loss for high-speed surface-mounted permanent magnet motor with rotor retaining sleeve [J]. *Transactions of China Electrotechnical Society*, 2022, 37

- (16): 4047-4059.
- [6] SUN R L, PENG H D, YANG D, et al. Analysis and research on loss and temperature rise of PMSMs using electromagnetic-thermal bi-directional coupling [J]. *Micro-motors*, 2022, 55(5): 23-29, 39.
- [7] CAO Y J, TAO S Q, YU L, et al. Analysis and calculation of winding eddy current loss in stator-coreless axial-flux permanent magnet machine [J]. *Journal of Southeast University*, 2016, 46(6): 1214-1220. (In Chinese)
- [8] LIU Q, LI J, ZHANG X W, et al. Design of giant magnetostrictive transducer and analysis of eddy current loss [J]. *Journal of Shaanxi Normal University*, 2022, 50(6): 64-68. (In Chinese)
- [9] LAN T, FENG P F, ZHANG J F, et al. Eddy current loss and thermal control of giant magnetostrictive transducer [J]. *Journal of Mechanical Engineering*, 2022, 58(21): 243-249.
- [10] CAI W C, FENG P F, YU D W, et al. Research on the optimization design method of prestress for giant magnetostrictive transducer [J]. *Journal of Vibration, Measurement and Diagnosis*, 2017, 37(1): 48-52, 198.
- [11] ZHU T, LI Z, LI Z, et al. Calculation of eddy current loss in permanent magnet synchronous motor based on analytical model [J]. *Journal of Shanghai University of Technology*, 2022, 44(5): 464-472. (In Chinese)
- [12] TANG R Y, CHEN P, TONG W M, et al. Analytical calculation of eddy current loss accounting for eddy current reaction [J]. *Transactions of China Electrotechnical Society*, 2015, 30(24): 1-10.
- [13] ZHANG F G, DU G H, WANG T Y, et al. Rotor strength analysis of high-speed permanent magnet under different protection measures [J]. *Proceedings of the CSEE*, 2013, 33(S1): 195-202.
- [14] BAI Y, CHEN X, LIU P, et al. Research on eddy-current loss of a permanent magnet high-speed solenoid valve [J]. *Transactions of CSICE*, 2022, 40(2): 179-185.
- [15] WANG X Y, LI H J, LIANG T Y, et al. Analysis of magnetic field and eddy current loss of permanent magnet starter/generator under field weakening condition [J]. *Proceedings of the CSU-EPSA*, 2022, 34(9): 81-87.
- [16] ZHANG D J, XIONG W L, LU L, et al. An analysis of rotor eddy current losses in high-speed and high-power PMSM [J]. *Computer Simulation*, 2017, 34(1): 236-240, 279.
- [17] XU Y X, HU J H, HU R Z, et al. An experimental verification method of calculation for rotor eddy current losses in PMSMs [J]. *Transactions of China Electrotechnical Society*, 2007(7): 150-154.
- [18] ZHAO J H, DU D Y, ZHANG B, et al. An electromagnetic-hydrostatic double supported radial bearing: ZL201710265591.9 [P]. 2018-12-07.
- [19] QIN B, LI S, ZHANG H, et al. Research on singular point characteristics and parameter bifurcation of single DOF nonlinear autonomous bearing system of magnetic-liquid double suspension bearing [J]. *International Journal of Hydromechanics*, 2023, 6(3): 179-218.

LIU Hongmei, born in 1988. She received her M. S. degree in mechanical engineering from Hebei University of Technology in 2014. She is currently working in Shijiazhuang Rail Transit Group Co. Ltd. She is mainly engaged in professional equipment of ventilation and air conditioning, water supply and drainage, and power distribution for rail transit.